



Insights into the intrinsic mechanisms underlying the ultra-highly efficient degradation of PFOA over S-scheme heterojunction of Bi₇O₅F₁₁/BiOF

Jingzhen Wang^{a,b}, Chun-Shuai Cao^{b,c}, Yinqing Zhang^b, Lingyan Zhu^{b,*}

^a College of Resources and Environment, Henan Agricultural University, Zhengzhou 450002, China

^b Key Laboratory of Pollution Processes and Environmental Criteria of Ministry of Education, Tianjin Key Laboratory of Environmental Remediation and Pollution Control, College of Environmental Science and Engineering of Nankai University, Tianjin 300350, China

^c Tianjin Key Laboratory of Green Chemical Technology and Process Engineering, and School of Chemistry, Tiangong University, Tianjin 300387, China

ARTICLE INFO

Keywords:

Perfluorooctanoic acid

S-scheme

In-situ

Layered structures

ABSTRACT

Perfluorooctanoic acid (PFOA) is refractory owing to the strong C-F bonds and is extremely difficult to be degraded by traditional photocatalysts. In this study, an S-scheme heterojunction was successfully synthesized by incorporating BiOF with wide-bandgap Bi₇O₅F₁₁. Theoretical calculations, in situ X-ray photoelectron spectroscopy and Kelvin probe force microscopy verified that a built-in electric field was created in the heterojunction, facilitating the separation of electron-hole pairs. Thus, the photoexcited electrons in the conduction-band (CB) of BiOF rapidly recombined with holes in the valence-band (VB) of Bi₇O₅F₁₁, leading to enrichment of the highly reductive electrons in CB of Bi₇O₅F₁₁ and strongly oxidative holes in VB of BiOF. Additionally, the strong interaction between Bi₇O₅F₁₁/BiOF and PFOA is conducive to electron transfer from catalyst surface to PFOA. Thus, BOF-2 displayed superbly-high photoactivity to decompose PFOA. PFOA (5 mg/L) was decomposed within 1 h, and 53% of total-organic-carbon was removed in 2 h of irradiation.

1. Introduction

Per- and polyfluoroalkyl substances (PFAS) have been used for several decades in many industrial and commercial applications, thus leading to their ubiquitous occurrence and detection in the environment [1]. Perfluorooctanoic acid (PFOA, C₇F₁₅COOH) is a common PFAS of primary concern and is the dominant PFAS homolog in the environment due to earlier regulations on its sulphonate counterpart, perfluorooctanesulfonic acid (PFOS) [2]. The strong electronegativity of F atoms and the strong carbon-fluorine bonds (bond energy 533 kJ·mol⁻¹) engender PFOA extremely resistant to decompose, gaining it the moniker “the forever chemical” [3,4]. Additionally, PFOA is ionic and highly soluble, which makes aquatic environments as its major sink. Therefore, it is frequently detected in tap water (ng/L), natural water bodies (ng/L–μg/L), and even in the blood of humans and wildlife [5–7]. A great number of studies documented that PFOA had various toxic effects, such as congenital disability, weakened immunity, growth retardation and so on [8,9]. In 2022, the United States Environmental Protection Agency (US EPA) established interim health advisory level of 0.02 ng/L for PFOS and 0.004 ng/L for PFOA in drinking water [10]. It is very challenging to develop highly efficient techniques to remove PFOA

from water to protect human health.

Several methods have been developed to remove or degrade PFOA in water, and among them photocatalysis is considered to be a prosperous solution considering its simple operation, high oxidation efficiency and environmental compatibility [11–13]. To ensure satisfactory photocatalytic performance to degrade PFOA, it is essential to design and fabricate photocatalysts with optimal band gap energy and band structure [11]. Among the many photocatalytic materials, bismuth oxyhalides (BiOX, X = F, Cl, Br, I) display attractive characteristics for PFOA degradation due to their unique two-dimensional layered structures and tunable energy-band properties [14,15]. In addition, the internal electric field (IEF) between halogen slabs and [Bi₂O₂] layers accelerate the charge migration and separation of electron-hole pairs, endorsing BiOX a good candidate for PFOA photocatalytic degradation [16].

Given the high energy C-F bonds in PFOA, it is generally considered that photocatalysts with broad energy-band would display better performance toward PFOA degradation [17]. BiOF, with a wide energy gap ($E_g \approx 3.5$ eV), has a high redox capacity of electron hole pairs generated by photoexcitation, and therefore is an excellent candidate [18,19]. Although BiOF has a high redox capacity, it is fairly difficult for single-component photocatalysts to realize rapid separation of

* Corresponding author.

E-mail address: zhuly@nankai.edu.cn (L. Zhu).

<https://doi.org/10.1016/j.apcatb.2023.122899>

Received 9 January 2023; Received in revised form 9 May 2023; Accepted 20 May 2023

Available online 31 May 2023

0926-3373/© 2023 Elsevier B.V. All rights reserved.

photogenerated carriers. Recently, construction of step scheme (S-scheme) heterojunctions, such as BiOBr/g-C₃N₄ [20], Bi₂Sn₂O₇/BiOBr [21], TiO₂/CsPbBr₃ [22], has been reported as a resultful strategy to overcome the aforementioned intrinsic shortcomings. In S-scheme heterojunctions, when two semiconductors with different Fermi levels (E_f) come into contact, electrons would flow from the semiconductor with higher E_f to that with low E_f until they reach balance at the interface [23], constructing an internal electric field (IEF) and causing band bending at the interface. This construction would drive effective separation of photoproduced charges, preserving the strongly oxidative h^+ and reductive e^- in the higher valence band (VB) and lower conduction band (CB), respectively. The detailed differences between S-scheme heterojunctions and the Z-scheme heterojunctions are summarized in Table S1 [24,25]. In our previous study [4], PFOA degradation was significantly improved by combining BiOF with the wide-band gap Metal-Organic Frameworks (MOFs) material. Bi₇O₅F₁₁ is a broadband gap semiconductor with outstanding performance, and it shares similar layered structure as BiOF [26–28]. It is anticipated that integrating them by in-situ synthesis might generate the most matching interface [29–31], which is more conducive to the flow of electrons and holes, and the internal electric field owned by Bi₇O₅F₁₁ and BiOF will also accelerate the electron transfer process [15].

Inspired by the above analyses, this study aims to develop a strategy for in situ synthesis of Bi₇O₅F₁₁/BiOF photocatalysts by controlling the strong coordination between Bi(III) and NH₄F and the reaction between Bi(III) and glycol to alkoxide. The regulation mechanism and principle of synthesis strategy are proposed and discussed. Meanwhile, the photocatalytic properties of the synthesized Bi₇O₅F₁₁/BiOF samples to degrade PFOA were systematically studied. The S-scheme mechanism of Bi₇O₅F₁₁/BiOF was discussed extensively according to theoretical calculation and in situ X-ray photoelectron spectroscopy (XPS) and in situ Kelvin probe force microscopy (KPFM). The dominant active species in the process of photoreaction were identified using trapping experiments and electron paramagnetic resonance (EPR) spectroscopy, and their attack ability was analyzed by theoretical calculation. The intermediate products of PFOA were identified by an ultra-performance liquid chromatography tandem mass spectrometry system (UPLC/MS/MS). The mechanisms of photoresist and decomposition pathway of PFOA were proposed.

2. Experimental section

2.1. Chemicals and reagents

Bi(NO₃)₃·5 H₂O was provided by McLean Biochemical Technology Co., Ltd, Shanghai, China. NH₄F was purchased from Tianjin University Kowei Co., Ltd, Tianjin, China. Ethylene glycol (EG) was afforded by Tianjin Balens Biotechnology Co. Ltd., China. The ammonium oxalate (AO), KBrO₃ and benzoquinone (BQ) were provided by Guangfu Technology Development Co. Ltd., Tianjin, China. The t-butanol and 5,5-dimethyl-1-pyrroline N-oxide (DMPO) were purchased from Aladdin Industrial Corporation, Shanghai, China. Acetic acid was supplied by Fuchen Chemical Reagent Co., Ltd, Tianjin, China. PFOA with > 99% purity was supplied by Wellington Laboratories, Guelph, Canada. Ultrapure water prepared by a Deirect-Pure UP ultrapure water system was used for all solutions (Shanghai Lefeng Biotechnology Co., Ltd, China).

2.2. Preparation of the photocatalysts

1. Preparation of Bi₇O₅F₁₁

Bi₇O₅F₁₁ was prepared using a hydrothermal method: 2 mmol of NH₄F and 1 mmol of Bi(NO₃)₃·5 H₂O were respectively dissolved in 15 mL of mixed solution of acetic acid and water (the volume ratio of acetic acid and water was 1:5), and labeled as solution A and B. After ultrasonication for 30 min, solution A was dropwise added into solution B under constant stirring. The mixture was then stirred for

another 30 min, and sealed in a 100 mL polytetrafluoroethylene (PTFE) reactor, which was heated in an oven at 160 °C for 24 h. Subsequently, the prepared material was collected by centrifugation after cooling down to about 25 °C naturally, and washed several times with deionized water and ethanol. Finally, the cleaned white material was placed in an oven at 80 °C and dried overnight to obtain Bi₇O₅F₁₁ photocatalyst.

2. Preparation of Bi₇O₅F₁₁/BiOF

In a typical procedure, 2 mmol Bi(NO₃)₃·5 H₂O was dissolved in 20 mL of ethylene glycol, and 2 mmol NH₄F was dissolved in 20 mL of ethylene glycol/H₂O mixed solutions, and the solutions were prepared under ultrasonication for 30 min. Next, the NH₄F solution was dropwise added to the Bi(NO₃)₃·5 H₂O solution, and the mixture was continuously stirred for another 30 min. The mixture was transferred to a 100 mL PTFE reactor, which was sealed and heated in an oven at 160 °C to react for 24 h. Thereafter, the solid products were collected by centrifugation and washed with deionized water and ethanol for several times. Finally, the greyish precipitates were placed in an oven at 80 °C to dry. For the prepared photocatalysts, when the solvent of NH₄F was pure water, the product was labeled as BOF-1; while other photocatalysts were labeled as BOF-2, BOF-3, BOF-4, and BOF-5 according to the volume ratio of water/ethylene glycol in NH₄F solvent (9:1, 7:3, 1:1, 3:7). The preparation process of Bi₇O₅F₁₁/BiOF photocatalyst was presented in Scheme 1.

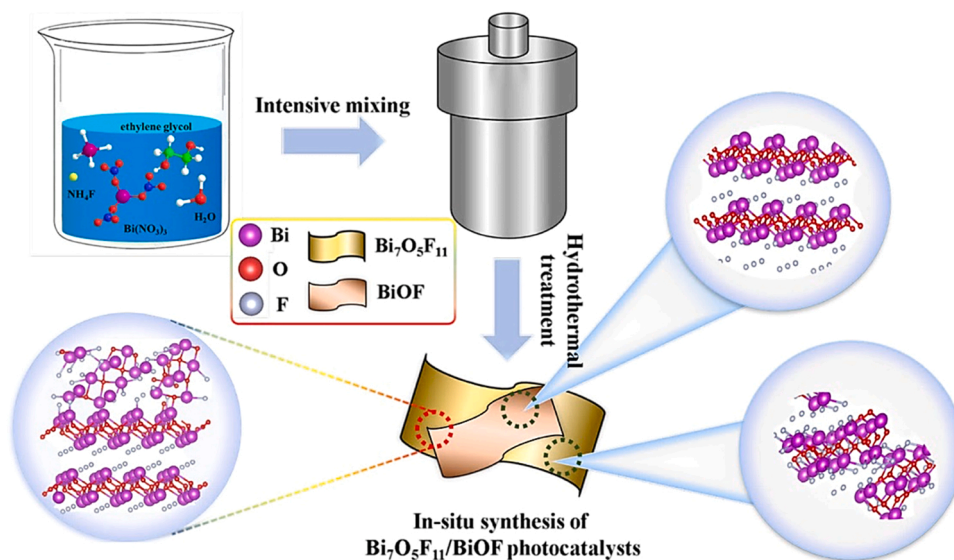
2.3. Characterization of the as-prepared photocatalysts

The crystal structures of the prepared Bi₇O₅F₁₁/BiOF composites were analyzed employing an Ultima IV X-ray diffractometer (XRD) by Cu-K α radiation under 40 kV and 100 mA with 8°/min from 5° to 80°. The morphology and microstructure of Bi₇O₅F₁₁/BiOF composites were inspected by JSM-7800 F field emission scanning electron microscopy (FESEM, Japan) and JEM-2800 high-resolution transmission electron microscopy (HRTEM, Japan). The chemical states, elemental compositions and charge transfer paths of the as-prepared photocatalysts were inspected by XPS and in situ XPS tests (XPS: ESCALAB250, Thermo Fisher Scientific, America). Kelvin probe force microscopy (KPFM) measurements were completed on a tap150E-G surface probe system (Bruker, Germany). The specific surface area and pore size distribution were determined by ASAP 2460 Brunauer-Emmett-Teller (BET, Micromeritics, America). Ultraviolet-visible diffuse reflection spectrophotometer (UV-vis DRS, U-3900 H, Techcomp, China) was used to measure the optical properties of Bi₇O₅F₁₁/BiOF composites with BaSO₄ as reference, and the scanning range was 200–800 nm. A total organic carbon analyzer (TOC Multi N/C3100, Analytic Jena, Germany) was applied to determine the content of total organic carbon in the degradation process of PFOA. The details of photoelectrochemical measurement, degradation experiments and PFOA analysis are shown in the Supporting information (SI).

3. Results and discussion

3.1. Characterization of the as-prepared Bi₇O₅F₁₁/BiOF

The XRD patterns of the as-prepared Bi₇O₅F₁₁/BiOF catalysts are shown in Fig. 1. The characteristic peaks of Bi₇O₅F₁₁ were marked by blue diamond in the composite materials. The peaks at 15.49°, 22.31°, 24.69°, 26.67°, 29.26°, 31.27° and 34.88° correspond to the ($\bar{2}01$), ($\bar{2}02$), (202), (112), (401), ($\bar{4}02$), (113) crystal facets of Bi₇O₅F₁₁, which are in agreement with those of pure Bi₇O₅F₁₁ phase (JCPDS card No. 97–016–7074). The diffraction peaks belonging to BiOF were marked with purple plum blossom pattern, and the labeled peaks correspond to (001), (101), (110), (102), (112), (200) and (211) planes of the standard [JCPDS No. 97–020–1620]. The characteristic peaks of the two standard cards were provided at the bottom of Fig. 1. It can be seen that the



Scheme 1. Scheme of the preparation procedure of $\text{Bi}_7\text{O}_5\text{F}_{11}/\text{BiOF}$.

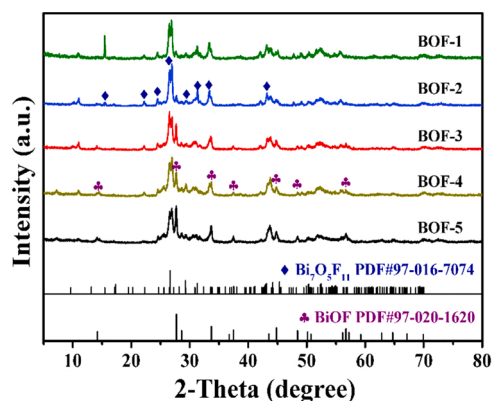


Fig. 1. XRD patterns of the as-prepared $\text{Bi}_7\text{O}_5\text{F}_{11}/\text{BiOF}$.

diffraction peak intensities of the prepared materials (from BOF-1 to BOF-5) belonging to $\text{Bi}_7\text{O}_5\text{F}_{11}$ gradually weakened, while those of BiOF increased obviously, particularly for the diffraction peak intensity of (101) crystal plane at 27.71° . This indicates that the BiOF content in the composite materials gradually increased while that of $\text{Bi}_7\text{O}_5\text{F}_{11}$ decreased with the increase of the volume ratio of water/ethylene glycol in NH_4F solvent.

In order to accurately analyze the relative contents of the two substances in the composite materials, the relative mass fractions of $\text{Bi}_7\text{O}_5\text{F}_{11}$ and BiOF in the composites were estimated according to the following equation [32]:

$$w_i = \frac{I_i / RIR_i}{\sum_{i=1}^N I_i / RIR_i}$$

where W_i is the mass fraction of phase i (%), I_i is the strongest integral intensity of phase i , RIR_i value from MDI Jade 9.0. As shown in Table S2, the calculated mass ratios of $\text{Bi}_7\text{O}_5\text{F}_{11}$ and BiOF in the composite materials of BOF-1 to BOF-5 were about 7:1, 3:1, 2:1 and 1:1. It is obvious that the mass ratio of $\text{Bi}_7\text{O}_5\text{F}_{11}$ and BiOF in the composites could be well modulated by simply tuning the volume ratio of water and ethylene glycol in the NH_4F precursor. It is worth noting that, when the volume ratio of water and ethylene glycol was 7:3 and 1:1, the mass ratio of $\text{Bi}_7\text{O}_5\text{F}_{11}$ and BiOF in the prepared composites was basically 2:1. It was speculated that the precursor compositions might affect the crystal

nucleation and growth. The possible growth mechanism was speculated as follows: In pure water system, a portion of the Bi(III) ions are prone to interact with ethylene glycol to form alkoxide, while the remaining Bi(III) ions are hydrolyzed to form BiONO_3 [33,34]. In the presence of NH_4F , a Bi-ammonia complex ($[\text{Bi}(\text{NH}_3)]^m$) may be generated because of the strong coordination capacity of NH_4F with Bi(III) ions [34]. With the increase of reaction temperature, the coordination complex could release Bi(III) ions gradually, which then reacted with F^- to form BiF_3 , while the accumulation of local BiF_3 will favor the formation of $\text{Bi}_7\text{O}_5\text{F}_{11}$ [33]. However, with the increase of ethylene glycol content in the reaction system, the hydrolysis of Bi(III) ions would be suppressed, leading to the reduced accumulation of local BiF_3 , which is manifested by the decreased relative mass of $\text{Bi}_7\text{O}_5\text{F}_{11}$ in the composites. Meanwhile, due to the large viscosity and integration of ethylene glycol, the growth process of materials was also suppressed in the hydrothermal process as the ethylene glycol became dominant. Ethylene glycol existing in a long chain structure under the action of hydrogen bonding can also be used as the growth template of BiOX, and then BiOX forms microsphere structure through self-assembly process [35]. Therefore, it was speculated that when the volume ratio of water and ethylene glycol was adjusted from 7:3–1:1, ethylene glycol may be sacrificed as the growth template, and thus the mass ratio of BOF-4 was similar to that of BOF-3. In order to verify this hypothesis, the morphologies of the as-prepared materials were characterized by SEM and HRTEM.

As shown in Fig. 2, the microstructure of the photocatalysts varied distinctly due to the different preparation conditions. Fig. 2a illustrates that BOF-1 was mainly in an aggregated granular morphology, with the particle size of about 50 nm. However, the BOF-2 photocatalyst was dominated by sheet structure of about 100 nm. With the increase of ethylene glycol content in the system, the prepared BOF-4 to BOF-5 were in perfect flower-like microspheres, which were mainly stacked with regular hexagonal lamellar structure. From the lamellar edge structure described in the inset of Fig. 2c, it could be clearly observed that the hexagonal lamellar structure formed in BOF-3 was relatively loose. Compared with BOF-3, the hexagonal lamellae in BOF-4 were squeezed more tightly, and they were interspersed more closely.

The morphology analysis of BOF-3 and BOF-4 confirmed the hypothesis that more ethylene glycol in the precursor solution of BOF-4 was consumed as a growth template, thus reducing the inhibitory effects of ethylene glycol on the generation of $\text{Bi}_7\text{O}_5\text{F}_{11}$. The flower-like stacked structure of BOF-4 composite was obtained. On the other hand, BOF-5 was completely self-assembled into flower-like microsphere, and the edge of lamellar structure was “multi-layer step” shape.

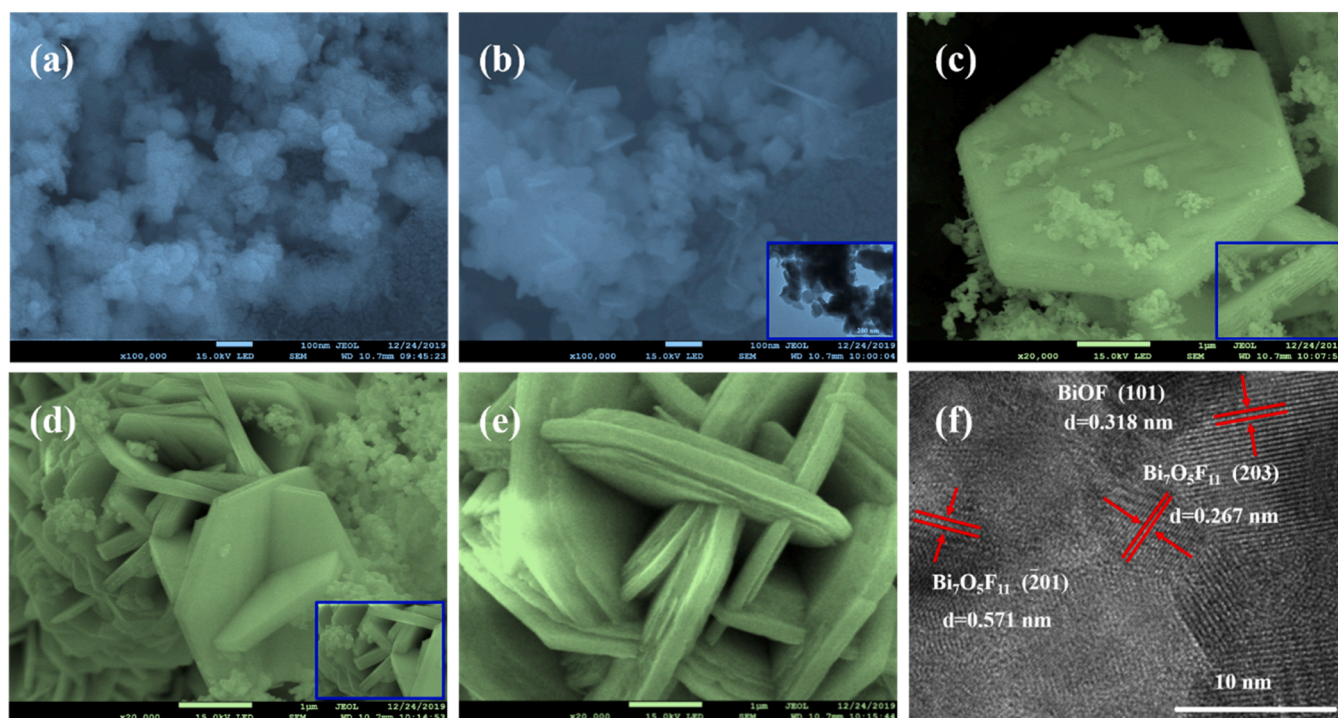


Fig. 2. SEM images of the prepared samples: (a) BOF-1, (b) BOF-2, (c) BOF-3, (d) BOF-4, (e) BOF-5; (f) HRTEM diagram of BOF-2.

As shown in Fig. 2f, the lattice spacings of 0.267 and 0.571 nm occurred on the edge corresponding to the (203) and (−201) facets of $\text{Bi}_7\text{O}_5\text{F}_{11}$, while that at 0.318 nm belongs to the (101) crystal plane of BiOF, which also strongly confirms that the product is composed of $\text{Bi}_7\text{O}_5\text{F}_{11}$ and BiOF.

The optical properties of the photocatalysts were characterized by the UV–vis diffusion reflectance spectra. As can be seen from Fig. S2, the photo-responses of the prepared composite photocatalysts were mainly in the range of 200–300 nm, and the absorption edges were between 350 nm and 370 nm. It was confirmed that they were responsive to ultraviolet light, which was also consistent with the characteristics of the band structure of the composites. Therefore, Hg lamp was selected as the light source for subsequent photocatalytic degradation experiments. In order to further understand the influence of mass ratio of $\text{Bi}_7\text{O}_5\text{F}_{11}$ and BiOF on the energy band structure, the band gap energies (E_g) of the prepared materials were calculated according to the equation of $(\alpha h\nu)^{1/n} = A(h\nu - E_g)$ ($n = 1/2$ or 2) [36,37]. Since both $\text{Bi}_7\text{O}_5\text{F}_{11}$ and BiOF were direct band gap semiconductors, the value of n was $1/2$ in the calculation process. The calculated band gap energies were as follows: $\text{BOF-1} < \text{BOF-2} < \text{BOF-3} < \text{BOF-4} = \text{BOF-5}$, which were 3.35 eV, 3.52 eV, 3.53 eV, 3.61 eV, respectively. The band gap energy of the composites shows an increasing trend with the decrease of the mass percentage of $\text{Bi}_7\text{O}_5\text{F}_{11}$ in the composites. A large band gap energy suggests that a higher excitation light energy is required, while the utilization rate of light energy decreases. However, the electron hole generated by these kinds of semiconductors equips with stronger redox ability [17].

The specific surface area, pore volume and pore size of the photocatalysts also directly affect their catalytic degradation activity. Large specific surface area can provide more reactive sites and facilitate the contact of contaminant molecules with the catalyst surface. The large pore volume and pore size may allow contaminant molecules to enter the pore structure, which facilitates the redox role of the photocatalysts. Therefore, the N_2 adsorption characteristics of the prepared photocatalysts were compared and summarized in Table S3. Compared with other composites, BOF-2 had the largest specific surface area, pore volume and pore diameter, which were $11.78 \text{ m}^2/\text{g}$, $0.0970 \text{ cm}^3/\text{g}$ and

60.41 nm respectively. In particular, the pore size was much larger than that of other composites, which was favorable for adequate contact between the photocatalysts and pollutant molecules.

In order to investigate the chemical states and valences of each element in the prepared composite photocatalysts, XPS characterization was carried out. As shown in Fig. S3, the $\text{Bi } 4f_{7/2}$ and $4f_{5/2}$ of all the materials were located at 159 eV and 164.3 eV, respectively, with an energy gap of 5.3 eV, which was in accordance with the valence state of Bi(III) in BOF [38]. As for O1s, two characteristic peaks were observed at 529.8 and 531.3 eV, which belong to lattice oxygen (Bi–O) and –OH absorbed on the surface (Fig. S3a). There were two binding peaks in the F 1s spectrum (Fig. S3b). The peak at 679.9 eV was corresponding to Bi 4p, while that at 683.3 eV was mainly originated from F 1s. The chemical bonds and existing chemical states of each element were similar in all the prepared materials although the mass ratio of $\text{Bi}_7\text{O}_5\text{F}_{11}$ and BiOF was different. All the orbital peaks of the five composites were basically consistent without obvious shift change, which indicates the co-growth of $\text{Bi}_7\text{O}_5\text{F}_{11}$ and BiOF during the synthesis process.

3.2. Photocatalytic performance on PFOA degradation

The photocatalytic properties of the prepared composite photocatalysts were investigated by the degradation of PFOA under UV light irradiation. All photocatalysts did not show significant difference in the adsorption properties to PFOA during the 60 min adsorption process. In the absence of photocatalyst, the removal rate of PFOA was basically negligible after 2 h of UV irradiation. As shown in Fig. 3a, the as-prepared BOF photocatalysts displayed more excellent photocatalytic performance compared with the commercial TiO_2 (the removal rate of PFOA after 2 h illumination is about 23%). The order of degradation efficiency was as follows: $\text{BOF-2} > \text{BOF-1} > \text{BOF-3} > \text{BOF-4} > \text{BOF-5}$. Among them, BOF-2 exhibited the highest photo-oxidation activity, which degraded 15 mg/L PFOA almost completely in 1 h. Based on Langmuir-Hinshelwood kinetics model, the first-order kinetics of PFOA photodegradation with all the employed photocatalysts are displayed in Fig. S4. Apparently, the degradation rate of PFOA ($k = 0.0459 \text{ min}^{-1}$) in the presence of BOF-2 was the highest, which was 2 and 41 times higher

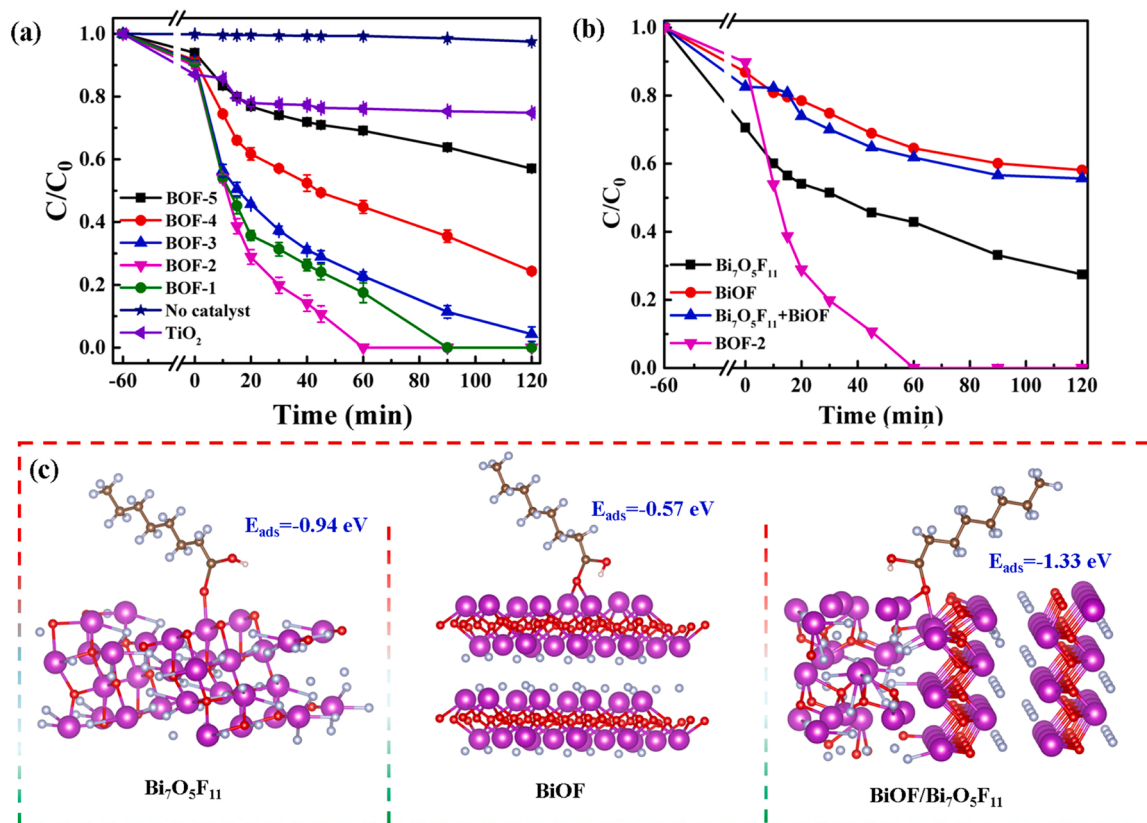


Fig. 3. (a) Photocatalytic properties of a series of photocatalysts ([PFOA] = 15 mg/L), (b) degradation performance curve of $\text{Bi}_7\text{O}_5\text{F}_{11}$, BiOF, $\text{Bi}_7\text{O}_5\text{F}_{11}$ + BiOF and BOF-2 for PFOA; (c) DFT calculated adsorption energy of PFOA on $\text{Bi}_7\text{O}_5\text{F}_{11}$, BiOF and $\text{Bi}_7\text{O}_5\text{F}_{11}$ /BiOF.

than that of BOF-1 ($k = 0.0223 \text{ min}^{-1}$) and commercial TiO_2 ($k = 0.0011 \text{ min}^{-1}$), respectively. Several kinds of photocatalysts have been fabricated for PFOA decomposition in previous studies, and Table S4 compared their efficiencies. It took much longer time ($>3 \text{ h} - 16 \text{ h}$) for these materials to photocatalytically degrade PFOA, but it took only 1 h for BOF-2 to remove 100% of PFOA. This suggests that BOF-2 exhibited ultra-high degradation performance to PFOA.

In order to verify that $\text{Bi}_7\text{O}_5\text{F}_{11}$ and BiOF mainly exert photocatalytic degradation through the interface interaction, rather than the simple mixing effect of the two substances, the pure substances of $\text{Bi}_7\text{O}_5\text{F}_{11}$ and BiOF were physically mixed in a mass ratio of 3:1 ($\text{Bi}_7\text{O}_5\text{F}_{11}$ + BiOF), and then reacted under the same degradation conditions. Indeed, as shown in Fig. 3b, BOF-2 exhibited much higher photocatalytic activity to degrade PFOA than those of $\text{Bi}_7\text{O}_5\text{F}_{11}$ + BiOF, pure $\text{Bi}_7\text{O}_5\text{F}_{11}$ and pure BiOF. This result magnifies that the intimate interfacial contact between $\text{Bi}_7\text{O}_5\text{F}_{11}$ and BiOF plays a critical role in the improvement of photocatalytic performance, which is an effect of "1 + 1 > 2". Thus, BOF-2 was selected as the representative catalyst in the subsequent degradation experiment, and the optimum reaction condition was determined as 0.5 g/L of BOF-2, 40 mL of PFOA (15 mg/L) under 120 min irradiation (Fig. S5).

The interaction between contaminant molecules and photocatalyst surface plays a crucial part in photocatalytic reaction. To understand the role of the catalyst surface in the chemisorption process, DFT analysis was carried out to investigate the chemisorption interactions between PFOA and photocatalyst at molecular level. The adsorption energy (E_{ads}) of PFOA on the $\text{Bi}_7\text{O}_5\text{F}_{11}$ /BiOF (-1.33 eV) was more negative than that on $\text{Bi}_7\text{O}_5\text{F}_{11}$ and BiOF (-0.94 eV and -0.57 eV, Fig. 3c) respectively, indicating that there was a much stronger interaction between the BOF-2 surface and PFOA, thus favoring the electron transfer from the surface of the $\text{Bi}_7\text{O}_5\text{F}_{11}$ /BiOF to PFOA, and the following degradation.

The reusability of BOF-2 during the photocatalytic degradation of

PFOA was tested. As shown in Fig. S7, the degradation rate of PFOA during the second and third cycles remained around 100%. After the recycle experiments, the BOF-2 was gathered and subjected to XRD analysis (Fig. S7b). The results indicated that the peak positions were well coincided with the original ones, demonstrating that it was very stable and resisted light erosion.

3.3. Photocatalytic mechanisms

In order to explore the roles of various active species involved in the photocatalytic degradation of PFOA by BOF-2, a couple of related scavengers were applied, including ammonium oxalate (AO) as scavengers for the photogenerated holes (h^+), KBrO₃, tertiary butanol (TBA) and p-benzoquinone (BQ) to trap photogenerated electrons (e^-), hydroxyl radicals ($\bullet\text{OH}$) and superoxide radicals ($\bullet\text{O}_2^-$), respectively [11]. As shown in Fig. 4a, the photocatalytic activity of BOF-2 was greatly suppressed by AO and BQ, and partly suppressed by KBrO₃. However, the effect of TBA was negligible. This manifested that the e^- , h^+ and $\bullet\text{O}_2^-$ played vital roles in PFOA decomposition by BOF-2. The results of the spin-trapping EPR measurement were consistent with those of the above experiments. TEMPO (2,2,6,6-tetramethylpiperidine-1-oxyl) was employed to monitor the generation of e^- and h^+ , because it is consumed by e^- and h^+ in carbonic acid and acetonitrile solutions, respectively, resulting in the decreased 1:1:1 characteristic signal of TEMPO [39]. As shown in Fig. 4(b-d), no corresponding free radical was detected in the three free radical detection systems without illumination. The signal intensities of e^- and h^+ gradually weakened due to consumption of TEMPO, while the signal peak intensity of $\bullet\text{O}_2^-$ increased with the extension of irradiation, indicating that e^- , h^+ and $\bullet\text{O}_2^-$ were generated and participated in the degradation process of PFOA.

In order to further promulgate the roles of various active species in the degradation of PFOA, the potential energy surface under the attack

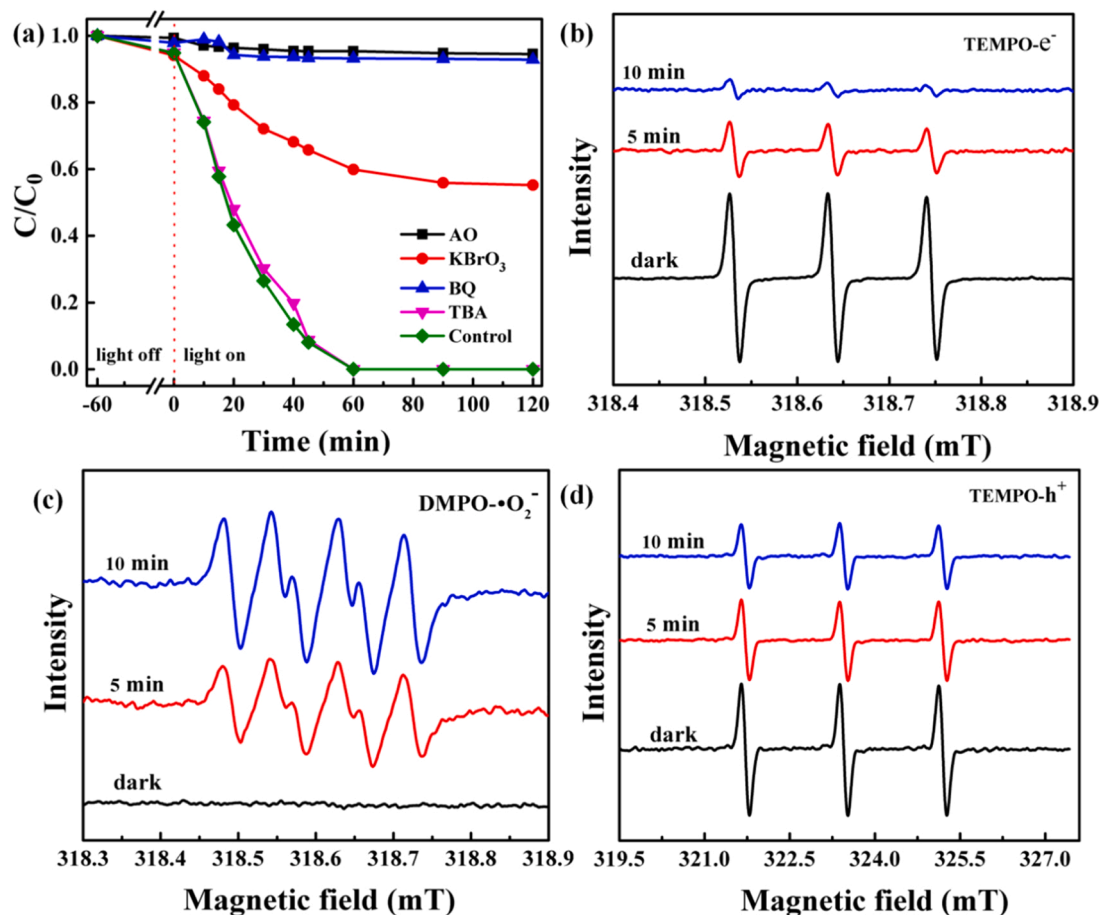


Fig. 4. (a) Trapping experiments of decomposing PFOA by add typical scavengers; EPR spectra of BOF-2 recorded for TEMPO-e^- (b), $\text{DMPO-}\bullet\text{O}_2^-$ (c) and TEMPO-h^+ (d) with different light irradiation time.

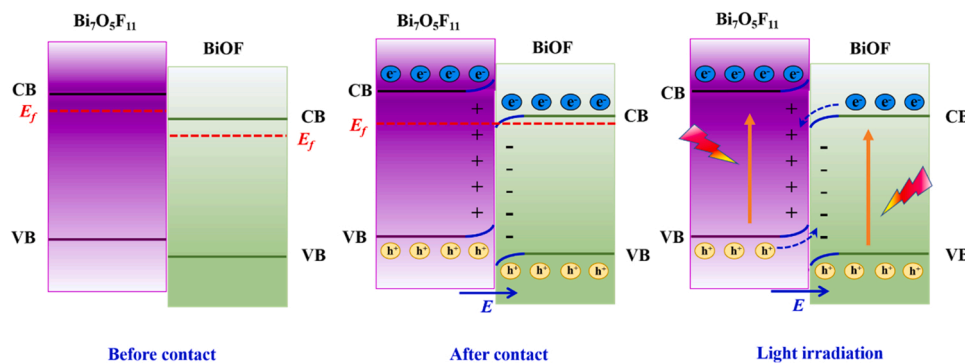
of different active species is plotted by DFT calculation. Fig. S8 presents the optimized geometries of the transition states, possible reaction pathways and the principal attack sites of PFOA under the attack of $\bullet\text{O}_2^-$, e^- and h^+ radicals according to our previous study [11]. The reaction barrier of $\bullet\text{O}_2^-$, h^+ and e^- is $24.78 \text{ kcal mol}^{-1}$, $18.98 \text{ kcal mol}^{-1}$ and $4.56 \text{ kcal mol}^{-1}$, respectively. Apparently, the attack of PFOA by electrons is the most thermodynamically favorable. Based on this, it is speculated that PFOA is firstly reduced by the photogenerated e^- , and then is decomposed under the joint action of $\bullet\text{O}_2^-$ and h^+ . On the other hand, $\bullet\text{O}_2^-$ and h^+ might also directly attack and decompose PFOA.

To explain the enhanced photocatalytic activity of the $\text{Bi}_7\text{O}_5\text{F}_{11}/\text{BiOF}$ composite, the band structures of $\text{Bi}_7\text{O}_5\text{F}_{11}$ and BiOF were evaluated by UV-vis DRS, Mott-Schottky plots and DFT calculations. The E_g values of $\text{Bi}_7\text{O}_5\text{F}_{11}$ and BiOF were 3.53 and 3.30 eV, respectively. Accordingly, the E_{CB} , E_{VB} and E_f values of $\text{Bi}_7\text{O}_5\text{F}_{11}$ and BiOF (the detailed calculation process is presented in SI) were calculated to be -1.15 , -0.47 , 2.38 , 2.83 , -0.95 and -0.27 eV, respectively. Fig. S10 reveals the band charge density distribution in $\text{Bi}_7\text{O}_5\text{F}_{11}/\text{BiOF}$. The highest occupied energy band (HOMO) is occupied by the $[\text{Bi}_2\text{O}_2]$ layers in BiOF bulk phase, while the lowest unoccupied energy band (LUMO) is occupied by $[\text{Bi}_2\text{O}_2]$ layers in the surface of BiOF and the interface region nearby $\text{Bi}_7\text{O}_5\text{F}_{11}$. The photogenerated electrons at HOMO could be easily excited to the LUMO as the $\text{Bi}_7\text{O}_5\text{F}_{11}/\text{BiOF}$ was exposed to light. According to the band structure parameters and the migration of photogenerated carriers determined by DFT calculations, the charges in the $\text{Bi}_7\text{O}_5\text{F}_{11}/\text{BiOF}$ complex mainly concentrated in $\text{Bi}_7\text{O}_5\text{F}_{11}$ while holes reserved in BiOF . This characteristic is different from that of the traditional type II heterojunction, suggesting it is an S-scheme heterojunction photocatalyst.

As displayed in Scheme 2, $\text{Bi}_7\text{O}_5\text{F}_{11}$ has a higher E_f than BiOF , when $\text{Bi}_7\text{O}_5\text{F}_{11}$ and BiOF contacted intimately, the e^- in $\text{Bi}_7\text{O}_5\text{F}_{11}$ transferred to BiOF until achieving a balanced E_f [24,25]. This charge transfer at the interface would induce formation of an IEF between the positively charged $\text{Bi}_7\text{O}_5\text{F}_{11}$ and negatively charged BiOF . Furthermore, the band edge of $\text{Bi}_7\text{O}_5\text{F}_{11}$ bends up due to loss of free electrons, while that of BiOF bends down due to enrichment of free electrons. Under light irradiation, both $\text{Bi}_7\text{O}_5\text{F}_{11}$ and BiOF are excited, the IEF and energy band bending drive the photogenerated e^- moving from the CB of BiOF to combine with h^+ in the VB of $\text{Bi}_7\text{O}_5\text{F}_{11}$, thus leading to formation of an S-scheme heterojunction between $\text{Bi}_7\text{O}_5\text{F}_{11}$ and BiOF .

In order to demonstrate the surface charge transfer pathway more accurately, in situ XPS tests were performed on BOF-2. As shown in Fig. 5, an increase in the binding energy of Bi elements and a decrease in the binding energy of O elements were observed, which may be caused by the transfer of charge from the BiOF surface to the $\text{Bi}_7\text{O}_5\text{F}_{11}$ surface under illumination. The 3D charge density difference was calculated to further probe the charge migration path and redistribution at the interface of $\text{Bi}_7\text{O}_5\text{F}_{11}/\text{BiOF}$. Fig. S10 illustrates that charges mainly transfer from BiOF bulk phase to $\text{Bi}_7\text{O}_5\text{F}_{11}$ via the interface, resulting in the accumulation of charges in $\text{Bi}_7\text{O}_5\text{F}_{11}$. Thus, the photogenerated electrons of BiOF bulk phase flow to $\text{Bi}_7\text{O}_5\text{F}_{11}$ surface rapidly, leaving the photogenerated holes at HOMO. The electric field direction was from the $\text{Bi}_7\text{O}_5\text{F}_{11}$ surface to the BiOF surface, which could accelerate the transfer of electrons at the interface [40]. As a consequence, the electron mobility is improved and separation of the e^- - h^+ pairs is facilitated, which further expounds the photocatalysis performance of $\text{Bi}_7\text{O}_5\text{F}_{11}/\text{BiOF}$ composites.

To further clarify the effect of IEF on the photoreactivity, the surface



Scheme 2. Schematic illustration of photocatalytic mechanism for BOF-2 composite under light irradiation.

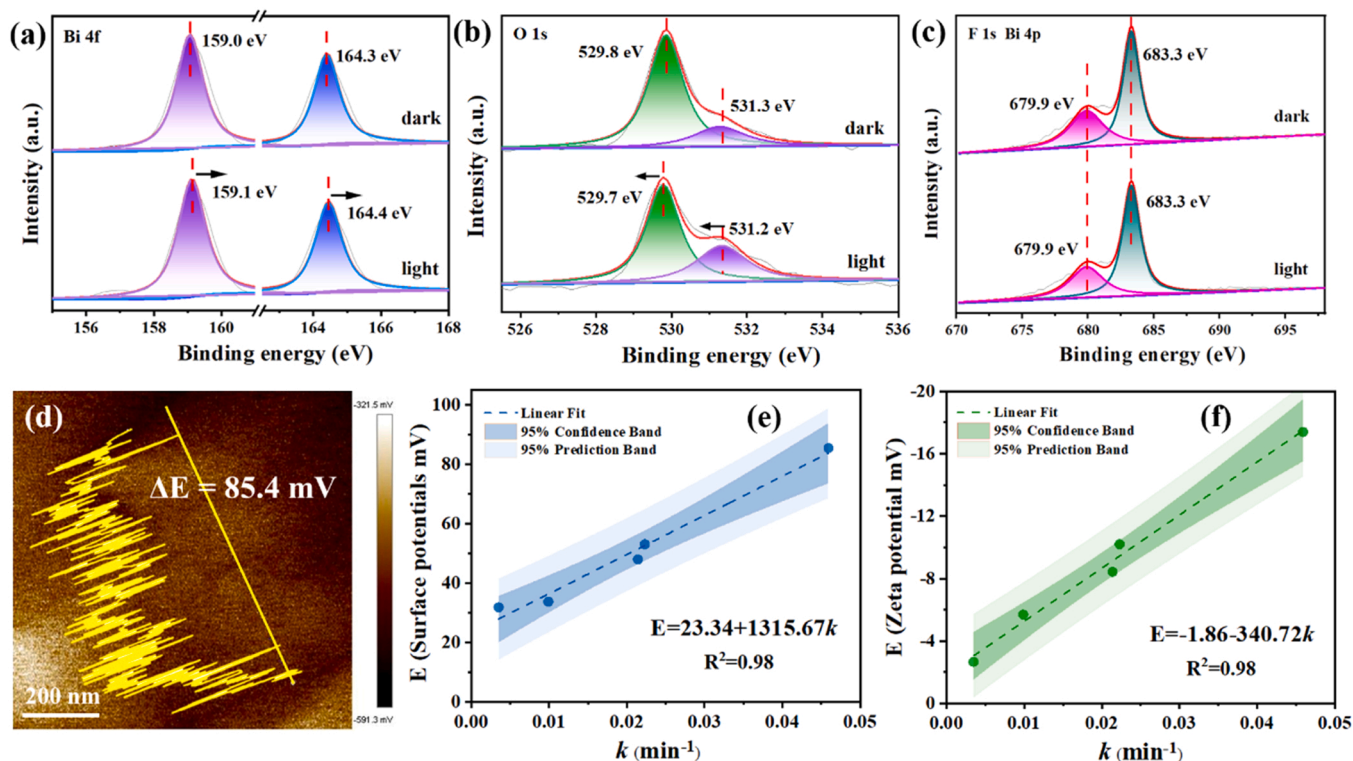


Fig. 5. In situ XPS fine spectrum of Bi 2 f (a), O 1 s (b) and F 1 s (c) in BOF-2; Surface potentials of BOF-2 (d); the linear relationship of the surface potentials (e) and Zeta potential (f) with rate constant k .

potentials and Zeta potential versus photoreactivity are qualitatively correlated and shown in Fig. 5(e, f). The IEF is reported to be proportional to the square root of the product of the surface potential and the surface charge density [41,42]. Kelvin probe force microscopy (KPFM) detects the surface potential. The surface potentials (ΔE) of BOF-1, BOF-2, BOF-3, BOF-4 and BOF-5 are approximately 53.1 mV, 85.4 mV, 48.0 mV, 33.8 mV and 31.9 mV (Fig. 5d and Fig. S11), respectively. BOF-2 exhibits the highest surface potential among the five kinds of BOFs. The surface charge density may be proportional to the Zeta potential [42]. The measured zeta potential changes (Table S5) were as follows: BOF-2 (-17.4 mV) > BOF-1 (-10.2 mV) > BOF-3 (-8.43 mV) > BOF-4 (-5.69 mV) > BOF-5 (-2.66 mV). BOF-2 again exhibits the largest Zeta potential, fortifying its highest surface charge density. In addition, the surface potentials and Zeta potential are positively correlated with the rate constant k , verifying that the enhancement of the IEF intensity is an essential factor in facilitating the performance of BOF-2.

The separation efficiency of the photoexcited electron-hole pairs was

further explored by photoluminescence spectroscopy (PL) and transient photocurrent response (PC). As shown in Fig. 6a, the PL spectra of the as-prepared $\text{Bi}_7\text{O}_5\text{F}_{11}/\text{BiOF}$ materials were analyzed at 325 nm excitation wavelength. There was a wide emission peak between 400 and 650 nm for all the materials. The emission intensity of the samples significantly decreased following the order of $\text{BOF-5} \approx \text{BOF-4} > \text{BOF-3} > \text{BOF-2}$, but then increased. Thus, the BOF-2 exhibited the weakest PL intensity among the prepared materials. In agreement with this, the transient photocurrent response of BOF-2 was much higher than that of other materials (Fig. 6b). These demonstrated that the electron-hole recombination rate of the BOF-2 was inhibited most efficiently, thereby prolonging the life time of the photogenerated-electrons, which was beneficial to the generation of $\bullet\text{O}_2^-$ radical and the improvement of photocatalytic performance.

3.4. Degradation pathway of PFOA

The calculation of mineralization rate by analyzing the removal rate

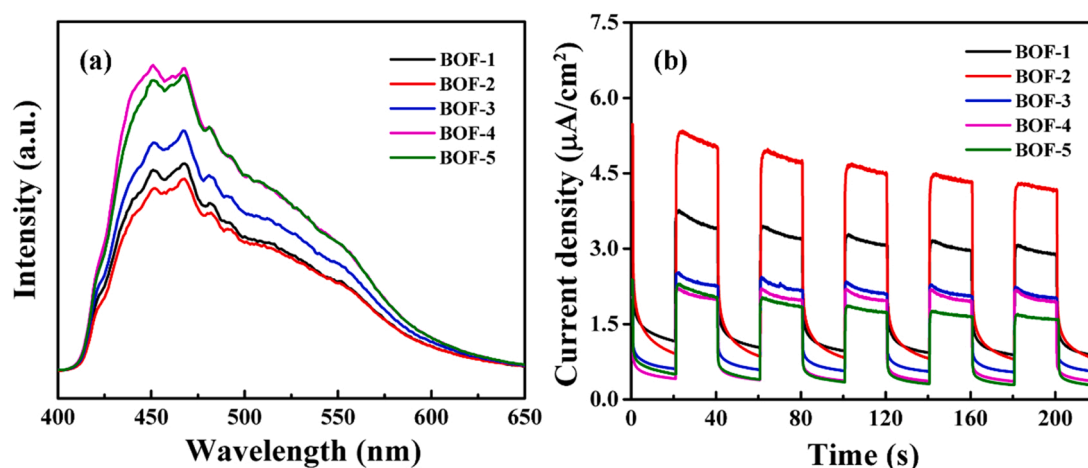


Fig. 6. PL spectra (a) and transient photocurrent response (b) of the as-prepared $\text{Bi}_7\text{O}_5\text{F}_{11}/\text{BiOF}$ materials.

of TOC in PFOA solution is of great significance to avoid secondary pollution in wastewater treatment. Fig. S12a displays that the removal rate of TOC increased with illumination time and reached 53% at 2 h. It was reported that the removal rate of TOC of PFOA by $\text{Pb-BFO}/0.5\%$ RGO system was only 28.0% after 8 h UV light irradiation [43]. In order to further analyze the specific process of PFOA decomposition, UPLC/MS/MS was used to explore the produced intermediates in the degradation process. A range of perfluorocarboxylic acids (PFCAs), including perfluorobutanoic acid (PFBA, $\text{C}_3\text{F}_7\text{COOH}$; $m/z = 213$), perfluoropentanoic acid (PFPeA, $\text{C}_4\text{F}_9\text{COOH}$; $m/z = 263$), perfluorohexanoic acid (PFHxA, $\text{C}_5\text{F}_{11}\text{COOH}$; $m/z = 313$) and perfluoroheptanoic acid (PFHpA, $\text{C}_6\text{F}_{13}\text{COOH}$; $m/z = 363$) were detected and quantified in the reaction solution (Fig. S13). As shown in Fig. S12b, the defluorination rate reached 29% within 2 h UV light irradiation, which proved that the C-F bonds were effectively destroyed. Song et al. [44] reported that the defluorination efficiency in PFOA degradation was 12% after 16 h of reaction with traditional $\text{Ti}_3\text{C}_2\text{-HF}/\text{TiO}_2$ as catalyst.

4. Conclusions

$\text{Bi}_7\text{O}_5\text{F}_{11}$ and BiOF have similar layered structures but different band structures, which were ingeniously used to fabricate a high-performance $\text{Bi}_7\text{O}_5\text{F}_{11}/\text{BiOF}$ photocatalyst. The hydrolysis of Bi(III) ions together with the coordination between Bi(III) ions and NH_4F were regulated to control the local BiF_3 accumulation in the composite. When the mass ratio of $\text{Bi}_7\text{O}_5\text{F}_{11}$ and BiOF was 3:1, the corresponding BOF-2 exhibited the most outstanding photocatalytic performance to complete degrade PFOA. This work further revealed that the introduction of a “build-in electric field” into the “S-scheme” photocatalyst has a strong driving force to enhance the performance of the composite photocatalyst. The reaction might be initiated by the reaction between PFOA and the highly reductive e^- generated by the irradiated BOF-2, then decomposed by h^+ , $\bullet\text{O}_2^-$. Attacked by these active species, PFOA was gradually mineralized by removing CF_2 units.

CRediT authorship contribution statement

Jingzhen Wang: Conceptualization, Investigation, Resources, Data curation, Writing – original draft. **Chun-Shuai Cao:** Conceptualization, Resources, Data curation. **Yinqing Zhang:** Supervision, Writing – review & editing. **Lingyan Zhu:** Conceptualization, Supervision, Writing – review & editing, Supervision, Project administration, Funding acquisition.

Declaration of Competing Interest

The authors declare that they have no known competing financial interests or personal relationships that could have appeared to influence the work reported in this paper.

Data Availability

Data will be made available on request.

Acknowledgements

This work was financially supported by National Natural Science Foundation of China (NSFC 41991313, 22106074, and 22111530176), Tianjin Natural Science Foundation (21JCZDJC00370, 20JCQNJC01840), the 111 Program of Ministry of Education, China (T2017002), Henan Natural Science Foundation (232300420377), the Special Fund for Topnotch Talents in Henan Agricultural University (30501306). We sincerely acknowledge the support and help from Prof. Weichao Wang (Nankai University) in DFT theoretical calculations.

Appendix A. Supporting information

Supplementary data associated with this article can be found in the online version at doi:10.1016/j.apcatb.2023.122899.

References

- [1] N. Ganbat, A. Altaee, J.L. Zhou, T. Lockwood, R.A. Al-Juboori, F.M. Hamdi, E. Karbassiyazdi, A.K. Samal, A. Hawari, H. Khabbaz, Investigation of the effect of surfactant on the electrokinetic treatment of PFOA contaminated soil, *Environ. Technol. Innov.* 28 (2022), 102938.
- [2] Z. Yang, K. Men, J. Guo, R. Liu, H. Liu, J. Wei, J. Zhang, L. Liu, X. Lin, M. Zhang, Y. Liu, Y. Chen, N.-j. Tang, Association between exposure to perfluoroalkyl substances and uric acid in Chinese adults, *Chemosphere* 312 (2023), 137164.
- [3] C. Chen, Y. Fang, X. Cui, D. Zhou, Effects of trace PFOA on microbial community and metabolisms: Microbial selectivity, regulations and risks, *Water Res.* 226 (2022), 119273.
- [4] J. Wang, C.-S. Cao, J. Wang, Y. Zhang, L. Zhu, Insights into highly efficient photodegradation of poly/perfluoroalkyl substances by In-MOF/BiOF heterojunctions: built-in electric field and strong surface adsorption, *Appl. Catal. B-Environ.* 304 (2022), 121013.
- [5] L.-N. Xie, X.-C. Wang, X.-J. Dong, L.-Q. Su, H.-J. Zhu, C. Wang, D.-P. Zhang, F.-Y. Liu, S.-S. Hou, B. Dong, G.-Q. Shan, X. Zhang, Y. Zhu, Concentration, spatial distribution, and health risk assessment of PFASs in serum of teenagers, tap water and soil near a Chinese fluorochemical industrial plant, *Environ. Int.* 146 (2021), 106166.
- [6] S. Fang, B. Sha, H. Yin, Y. Bian, B. Yuan, I.T. Cousins, Environment occurrence of perfluoroalkyl acids and associated human health risks near a major fluorochemical manufacturing park in southwest of China, *J. Hazard. Mater.* 396 (2020), 122617.

- [7] Z. Zhang, F. Wang, Y. Zhang, J. Yao, J. Bi, J. He, S. Zhang, Y. Wei, H. Guo, X. Zhang, M. He, Associations of serum PFOA and PFOS levels with incident hypertension risk and change of blood pressure levels, *Environ. Res.* 212 (2022), 113293.
- [8] L. Liang, Y. Pan, L. Bin, Y. Liu, W. Huang, Rong Li, K.P. Lai, Immunotoxicity mechanisms of perfluorinated compounds PFOA and PFOS, *Chemosphere* 291 (2022), 132892.
- [9] L. Darrow, A. Groth, A. Winquist, H. Shin, S. Bartell, K. Steenland, Modeled perfluorooctanoic acid (PFOA) exposure and liver function in a Mid-Ohio valley community, *Environ. Health Perspect.* 124 (2016) 1227–1233.
- [10] J.E.F. Abraham, K.G. Mumford, D.J. Patch, K.P. Weber, Retention of PFOS and PFOA mixtures by trapped gas bubbles in porous media, *Environ. Sci. Technol.* 56 (2022) 15489–15498.
- [11] J. Wang, C. Cao, Y. Zhang, Y. Zhang, L. Zhu, Underneath mechanisms into the super effective degradation of PFOA by BiOF nanosheets with tunable oxygen vacancies on exposed (101) facets, *Appl. Catal. B-Environ.* 286 (2021), 119911.
- [12] S. Dong, X. Ding, T. Guo, X. Yue, X. Han, J. Sun, Self-assembled hollow sphere shaped Bi₂WO₆/RGO composites for efficient sunlight-driven photocatalytic degradation of organic pollutants, *Chem. Eng. J.* 316 (2017) 778–789.
- [13] S. Dong, L. Cui, W. Zhang, L. Xia, S. Zhou, C.K. Russell, M. Fan, J. Feng, J. Sun, Double-shelled ZnSnO₃ hollow cubes for efficient photocatalytic degradation of antibiotic wastewater, *Chem. Eng. J.* 384 (2020), 123279.
- [14] Y. Yang, C. Zhang, C. Lai, G. Zeng, D. Huang, M. Cheng, J. Wang, F. Chen, C. Zhou, W. Xiong, BiOX (X = Cl, Br, I) photocatalytic nanomaterials: applications for fuels and environmental management, *Adv. Colloid Interface* 254 (2018) 76–93.
- [15] Y. Zhao, H. Guo, J. Liu, Q. Xia, J. Liu, X. Liang, E. Liu, J. Fan, Effective photodegradation of rhodamine B and levofloxacin over CQDs modified BiOCl and BiOBr composite: mechanism and toxicity assessment, *J. Colloid Interface Sci.* 627 (2022) 180–193.
- [16] Z.-H. He, B.-T. Wu, Z.-Y. Wang, S.-Y. Yang, K. Wang, J.-J. Shi, M.-X. He, W. Wang, Z.-T. Liu, Photothermal catalytic CO₂ oxidative dehydrogenation of propane to propylene over BiOX (X = Cl, Br, I) nanocatalysts, *Green. Chem.* 24 (2022) 8270–8279.
- [17] L. Duan, B. Wang, K. Heck, S. Guo, C.A. Clark, J. Arredondo, M. Wang, T.P. Senftle, P. Westerhoff, X. Wen, Y. Song, M.S. Wong, Efficient photocatalytic PFOA degradation over boron nitride, *Environ. Sci. Technol. Lett.* 7 (2020) 613–619.
- [18] M. Nasr, W. Huang, C. Bittencourt, D. Cui, Y. Sun, L. Wang, N.G. Caperaa, Y. Ning, P. Song, P. Bonnet, C. Wang, Synthesis of BiOF/TiO₂ heterostructures and their enhanced visible-light photocatalytic activity, *Eur. J. Inorg. Chem.* 2020 (2020) 253–260.
- [19] S. Vadivel, V.P. Kamalakannan, N.P. Kavitha, T. Santhoshini Priya, N. Balasubramanian, Development of novel Ag modified BiOF squares/g-C₃N₄ composite for photocatalytic applications, *Mater. Sci. Semicond. Process.* 41 (2016) 59–66.
- [20] X. Jia, C. Hu, H. Sun, J. Cao, H. Lin, X. Li, S. Chen, A dual defect co-modified S-scheme heterojunction for boosting photocatalytic CO₂ reduction coupled with tetracycline oxidation, *Appl. Catal. B-Environ.* 324 (2023), 122232.
- [21] Y. Zhang, J. Di, X. Zhu, M. Ji, C. Chen, Y. Liu, L. Li, T. Wei, H. Li, J. Xia, Chemical bonding interface in Bi₂Sn₂O₇/BiOBr S-scheme heterojunction triggering efficient N₂ photofixation, *Appl. Catal. B-Environ.* 323 (2023), 122148.
- [22] F. Xu, K. Meng, B. Cheng, S. Wang, J. Xu, J. Yu, Unique S-scheme heterojunctions in self-assembled TiO₂/CsPbBr₃ hybrids for CO₂ photoreduction, *Nat. Commun.* 11 (2020) 1–9.
- [23] H. Ren, F. Qi, A. Labidi, J. Zhao, H. Wang, Y. Xin, J. Luo, C. Wang, Chemically bonded carbon quantum dots/Bi₂WO₆ S-scheme heterojunction for boosted photocatalytic antibiotic degradation: interfacial engineering and mechanism insight, *Appl. Catal. B-Environ.* 330 (2023), 122587.
- [24] Q. Xu, L. Zhang, B. Cheng, J. Fan, J. Yu, S-Scheme heterojunction photocatalyst, *Chem* 6 (2020) 1543–1559.
- [25] B. Xia, B. He, J. Zhang, L. Li, Y. Zhang, J. Yu, J. Ran, S. Qiao, TiO₂/FePS₃ S-Scheme heterojunction for greatly raised photocatalytic hydrogen evolution, *Adv. Energy Mater.* 12 (2022), 2201449.
- [26] Y. Kan, F. Teng, Y. Yang, J. Xu, L. Yang, Direct conversion mechanism from BiOCl nanosheets to BiOF, Bi₇F₁₁O₅ and BiF₃ in the presence of a fluorine resource, *RSC Adv.* 6 (2016) 63347–63357.
- [27] L.S. Gómez-Velázquez, A. Hernández-Gordillo, M.J. Robinson, V.J. Leppert, S. E. Rodil, M. Bizarro, The bismuth oxyhalide family: thin film synthesis and periodic properties, *Dalton Trans.* 47 (2018) 12459–12467.
- [28] D. Wei, Y. Huang, H.-J. Seo, Eu³⁺-doped Bi₇O₅F₁₁ microplates with simultaneous luminescence and improved photocatalysis, *Appl. Mater.* 8 (2020), 081109.
- [29] L. Chen, X.-L. Song, J.-T. Ren, Z.-Y. Yuan, Precisely modifying Co₂P/black TiO₂ S-scheme heterojunction by in situ formed P and C dopants for enhanced photocatalytic H₂ production, *Appl. Catal. B-Environ.* 315 (2022), 121546.
- [30] J.-T. Ren, G.-G. Yuan, L. Chen, C.-C. Weng, Z.-Y. Yuan, Rational dispersion of Co₂P₂O₇ fine particles on N,P-codoped reduced graphene oxide aerogels leading to enhanced reversible oxygen reduction ability for Zn-air batteries, *ACS Sustain. Chem. Eng.* 6 (2018) 9793–9803.
- [31] L. Chen, J.-T. Ren, Z.-Y. Yuan, Insight into the active contribution of N-coordinated cobalt phosphate nanocrystals coupled with carbon nanotubes for oxygen electrochemistry, *ACS Sustain. Chem. Eng.* 9 (2021) 1856–1866.
- [32] C. Chang, L. Zhu, Y. Fu, X. Chu, Highly active Bi/BiOI composite synthesized by one-step reaction and its capacity to degrade bisphenol A under simulated solar light irradiation, *Chem. Eng. J.* 233 (2013) 305–314.
- [33] N. Garti, H. Zour, The effect of surfactants on the crystallization and polymorphic transformation of glutamic acid, *J. Cryst. Growth* 172 (1997) 486–498.
- [34] M. Ren, F. Teng, Y. Yang, Y. Zhai, W. Gu, Z. Liu, Z. Liu, Y. Teng, Influence of O/F ratio on oxygen defect and photochemical properties of Bi_xO_yF_z, *Mater. Des.* 131 (2017) 402–409.
- [35] W. Zhao, H. Wang, N. Liu, J. Rong, Q. Zhang, M. Li, X. Yang, Hydrothermal synthesis of litchi-like SrTiO₃ with the help of ethylene glycol, *J. Am. Ceram. Soc.* 102 (2019) 981–987.
- [36] J. Tauc, R. Grigorovici, A. Vancu, Optical properties and electronic structure of amorphous germanium, *Phys. Stat. Sol.* 627 (1966) 627–637.
- [37] L. Zhou, Z. Liu, Z. Guan, B. Tian, L. Wang, Y. Zhou, Y. Zhou, J. Lei, J. Zhang, Y. Liu, 0D/2D plasmonic Cu₂-xS/g-C₃N₄ nanosheets harnessing UV–vis–NIR broad spectrum for photocatalytic degradation of antibiotic pollutant, *Appl. Catal. B-Environ.* 263 (2020), 118326.
- [38] H. Wu, Z. Hu, R. Liang, O.V. Nkwachukwu, O.A. Arotiba, M. Zhou, Novel Bi₂Sn₂O₇ quantum dots/TiO₂ nanotube arrays S-scheme heterojunction for enhanced photoelectrocatalytic degradation of sulfamethazine, *Appl. Catal. B-Environ.* 321 (2023), 122053.
- [39] H. Wang, W. Cui, X. Dong, J. Li, Q. Chen, Z. Wang, Y. Sun, J. Sheng, Y. Zhou, Y. Zhang, F. Dong, Interfacial activation of reactants and intermediates on CaSO₄ insulator based heterostructure for efficient photocatalytic NO removal, *Chem. Eng. J.* 390 (2020), 124609.
- [40] Y. Lin, C. Yang, S. Wu, X. Li, Y. Chen, W.L. Yang, Construction of built-in electric field within silver phosphate photocatalyst for enhanced removal of recalcitrant organic pollutants, *Adv. Funct. Mater.* 30 (2020), 2002918.
- [41] T. Kanata-Kito, M. Matsunaga, H. Takakura, Y. Hamakawa, T. Nishino, F. Pollak, M. Cardona, D. Aspnes, Photoreflectance characterization of built-in potential in MBE-produced as-grown GaAs surface, *Proc. SPIE* 1286 (1990) 56–65.
- [42] Y. Zhang, D. Wang, W. Liu, Y. Lou, Y. Zhang, Y. Dong, J. Xu, C. Pan, Y. Zhu, Create a strong internal electric-field on PDI photocatalysts for boosting phenols degradation via preferentially exposing π -conjugated planes up to 100%, *Appl. Catal. B-Environ.* 300 (2022), 120762.
- [43] E. Shang, Y. Li, J. Niu, S. Li, G. Zhang, X. Wang, Photocatalytic degradation of perfluorooctanoic acid over Pb-BiFeO₃/rGO catalyst: Kinetics and mechanism, *Chemosphere* 211 (2018) 34–43.
- [44] H. Song, Y. Wang, Z. Ling, D. Zu, Z. Li, Y. Shen, C. Li, Enhanced photocatalytic degradation of perfluorooctanoic acid by Ti₃C₂ MXene-derived heterojunction photocatalyst: application of intercalation strategy in DESS, *Sci. Total. Environ.* 746 (2020), 141009.